



ASME Accepted Manuscript Repository

Institutional Repository Cover Sheet

Michele Sergio

Campobasso

First

Last

ASME Paper Title: Computational Fluid Dynamics Analysis of Floating Offshore Wind Turbines in Severe

Pitching Conditions

Authors: A. Ortolani, G. Persico, J. Drofelnik, A. Jackson, M.S. Campobasso

ASME Journal Title: Journal of Engineering for Gas Turbines and Power

Volume/Issue 142/12

Date of Publication (VOR* Online) 15 March 2016

ASME Digital Collection URL: _____

<https://asmedigitalcollection.asme.org/gasturbinespower/article-abstract/142/12/121003/1088420/Computational-Fluid-Dynamics-Analysis-of-Floating?redirectedFrom=fulltext>

DOI: 10.1115/1.4048776

ASME ©; CC-BY distribution license

*VOR (version of record)

Computational Fluid Dynamics Analysis of Floating Offshore Wind Turbines in Severe Pitching Conditions

Andrea Ortolani

Dipartimento di Energia
Politecnico di Milano
Via Lambruschini 4
20156-Milano, Italy

Email: andrea.ortolani@mail.polimi.it

Giacomo Persico

Dipartimento di Energia
Politecnico di Milano
Via Lambruschini 4
20156-Milano, Italy

Email: giacomo.persico@polimi.it

Jernej Drofelnik

Pipistrel Vertical Solutions d.o.o.
Vipavska cesta 2
SI-5270 Ajdovščina, Slovenia
Email: jernej.drofelnik@pipistrel.si

Adrian Jackson

University of Edinburgh, EPCC
Edinburgh EH9 3JZ, United Kingdom
Email: adrian.jackson@ed.ac.uk

M. Sergio Campobasso*

University of Lancaster, Department of Engineering
Lancaster LA1 4YR, United Kingdom
Email: m.s.campobasso@lancaster.ac.uk

ABSTRACT

The unsteady aerodynamics of floating wind turbines is more complex than that of fixed-bottom turbines, and the uncertainty of low-fidelity predictions is higher for floating turbines. Navier–Stokes Computational Fluid Dynamics (CFD) can improve the understanding of rotor and wake aerodynamics of floating turbines, and help improving lower-fidelity models. Here, the flow field of the NREL 5 MW rotor with fixed tower, and subjected to prescribed harmonic pitching past the tower base are investigated using blade-resolved CFD compressible flow COSA simulations and incompressible flow FLUENT simulations. CFD results are also compared to predictions of the FAST

*Corresponding author.

wind turbine code, which uses blade element momentum theory (BEMT). The selected rotor pitching parameters correspond to an extreme regime unlikely to occur without faults of the turbine safety system, and thus relevant to extreme aerodynamic load analysis. The rotor power and loads in fixed-tower mode predicted by both CFD codes and BEMT are in very good agreement. For the floating turbine, all predicted periodic profiles of rotor power and thrust are qualitatively similar, but the power peaks of both CFD predictions are significantly higher than those of BEMT. Moreover, cross-comparisons of the COSA and FLUENT predictions of blade static pressure also highlight significant compressible flow effects on rotor power and loads. The CFD analyses of the downstream rotor flow also reveal wake features unique to pitching turbines, primarily the space- and time-dependence of the wake generation strength, highlighted by intermittency of the tip vortex shedding.

1 INTRODUCTION

Wind energy plays a key role in reducing greenhouse gas emissions due to electric power generation. This is due to both the abundance of this renewable energy resource, and the fact that the level of maturity of the wind energy conversion technology is enabling increasingly large reductions of its levelized cost of energy (LCOE). Indeed, onshore wind LCOE has become lower than that of fossil fuel electricity generation, and the growing technological and commercial investment of many countries in offshore wind is expected to make offshore wind LCOE competitive with that of fossil fuel in the near future. The presently dominant technology for harvesting offshore wind is based on fixed-bottom turbines, whose foundations are economically affordable for water depths of less than about 50 meters. In deeper waters, the use of floating offshore wind turbines (FOWTs), *i.e.* turbines mounted on moored floaters, is required.

Rotor flows of onshore and fixed-bottom offshore horizontal axis wind turbines (HAWTs) are inherently unsteady due to several environmental factors, such as atmospheric turbulence, vertical wind shear and density stratifications, aerodynamic influence of the tower, and temporary misalignment of wind direction and rotor axis (yaw errors). FOWT rotor flows are subjected to an additional major source of unsteadiness, namely that resulting from the rigid body motion induced by the relatively large tower motion enabled by its softer foundations [1], *i.e.* the moored floater. The overall FOWT dynamics is determined by the dynamic equilibrium of several concurrent loads, including the aerodynamic and gravitational forces on the rotor blades, the wave, current and mooring loads on the floating platform, and the inertial forces of all FOWT components. The reliable and optimized design of FOWTs capable of operating with minimum maintenance in the harsh offshore environment for 20+ years requires accurate predictions of all aforementioned loads, including the aerodynamic ones, whose analysis is the main focus of this study. Reliable predictions of the aerodynamic loads are key to providing the fatigue and extreme loads required for the system structural design, analyzing and optimizing FOWT hydrodynamic stability, and designing the turbine control, often tasked with providing additional damping to improve hydrodynamic stability.

FOWT rotor aerodynamics is often analyzed with low-fidelity models such as the Blade Element Momentum Theory (BEMT) [2]. BEMT codes result from combining the principle of conservation of linear and angular momentum with classical lift and drag theory. The baseline approach is two-dimensional, with three-dimensional (3D) and unsteady flow effects accounted for by means of semi-empirical correlations. BEMT codes are computationally fast, and well validated

for utility-scale HAWT analysis and design. Their use for FOWT applications, however, is affected by an as-yet undefined level of uncertainty, arising because state-of-the-art BEMT codes have been fine-tuned for fixed-bottom rotors and not for FOWT rotors, whose aerodynamics is made more complex by the additional entrainment speeds due to the tower motion [3]. Promising low-fidelity alternative methods, which incorporate some more physics than BEMT codes (particularly with regard to wake dynamics) and have been recently used for FOWT aerodynamic analyses, include free-vortex methods (FVMs) [4,5]. FVMs assume incompressible, inviscid and irrotational flow; like BEMT codes, they do not resolve the blade geometry and its 3D and unsteady aerodynamics, as they model the blade forces using lifting lines. Their execution speed is still fairly high, and they can achieve a good trade-off between solution reliability and computational efficiency.

High-fidelity Navier-Stokes (NS) Computational Fluid Dynamics (CFD) has been successfully used to analyze in great detail the unsteady flow physics of fixed-bottom turbines [6], and the technology has the potential of resolving with high reliability the complex unsteady aerodynamics of FOWT rotors. However, even the predictions of high-fidelity CFD may be affected by some uncertainty, particularly in the analysis of unsteady rotor flows caused by complex system kinematics, such as that associated with the relatively large motion of FOWTs. Therefore, the availability of measured data of FOWT rotor flow fields [7] for CFD code validation constitutes a valuable means to further improve confidence in CFD analyses, and use their findings to improve low-fidelity codes for FOWT analysis and design.

To assess the correlation of CFD and low-fidelity BEMT predictions of FOWT rotor aerodynamics, Tran and Kim analyzed the unsteady aerodynamics of a pitching FOWT rotor [8] with different motion parameters using the ANSYS FLUENT CFD code and several BEMT codes. They found that the agreement of low- and high-fidelity predictions in terms of peak rotor power and thrust worsened with the severity of the pitching motion. They also studied the unsteady aerodynamics of a surging FOWT rotor [9], using the STAR-CCM+ CFD code with overset grids and the BEMT approach, and more general FOWT motions [10] using a strongly coupled aerodynamic/hydrodynamic high-fidelity CFD framework and the NREL wind turbine code FAST [11]. Also in these cases, they found that the agreement of high- and low-fidelity results worsened with the severity of the operating regime. Liu *et al.* [12] studied FOWT dynamics including rotor aerodynamics, floater hydrodynamics, and mooring dynamics. Their study used a multi-disciplinary high-fidelity and fully coupled approach based on the incompressible OpenFOAM solver, and compared the high-fidelity results to those of FAST. A good agreement of the two approaches was reported. A comprehensive compressible flow analysis of FOWT rotor aerodynamics for the pitching and surging cases was provided in [13], which included detailed FOWT rotor wake analyses.

Compressibility effects are likely to play a significant role in FOWT aerodynamics. The sheer size of FOWTs and the entrainment velocity due the floater motion result in large time-dependent variations of the relative angle of attack (AoA) to the rotor blades. In turn, these higher AoA values may result in relative Mach numbers past the blades exceeding the compressible limit of 0.3. Both incompressible and compressible solvers are used in wind turbine aerodynamics [14, 15], but a systematic comparison of incompressible and compressible CFD codes for FOWT aerodynamics is as yet unavailable. Initial investigations into this aspect were reported in [16], which presented the first application of the compressible COSA code to a pitching FOWT and comparisons with FAST predictions.

This report presents new COSA simulations of the pitching FOWT rotor studied in [16], and thoroughly compares these

results with incompressible flow FLUENT simulations performed using the same mesh, and NREL FAST predictions. The selected pitching parameters correspond to an extreme FOWT motion regime which may occur if faults of the turbine safety system prevented turbine shut-down. Hence, the considered turbine kinematics is relevant to testing aerodynamic codes for extreme load analysis.

The key novel features of this work are a) a comprehensive quantitative investigation into the impact of flow compressibility on the performance of pitching FOWT rotors, b) a cross-comparative analysis of high-fidelity CFD and low-fidelity BEMT-based FOWT rotor aerodynamic predictions, including a discussion on the possible causes of and remedies to the discrepancies between high- and low-fidelity results, and c) a detailed analysis of the main features of pitching FOWT wake and tip vortex generation, enabled by the use of blade-resolved CFD simulations. The flow problem formulation and the details of the two CFD set-ups are discussed first. Then the steady high- and low-fidelity simulations of the fixed-tower rotor flow field are compared. This is followed by cross-comparative analyses of high- and low-fidelity FOWT rotor performance predictions, and the CFD analysis of the FOWT rotor wake. A summary is provided in the closing section.

2 GOVERNING EQUATIONS

The 3D compressible RANS equations are a system of conservation laws expressing the conservation of mass, momentum and energy in a turbulent fluid flow. The effects of turbulence on the mean flow field are accounted for by introducing the Reynolds stress tensor in the momentum and energy equations. Here this tensor is modeled using Menter's two-equation $k - \omega$ shear stress transport (SST) turbulence model [17, 18], a linear eddy viscosity model. Thus, using the compressible flow model, turbulent flows are determined by solving a system of seven partial differential equations (PDEs) and an equation of state linking fluid density, pressure and internal energy.

Given a moving control volume C with boundary S , the Arbitrary Lagrangian-Eulerian (ALE) integral form of the system of the time-dependent (TD) RANS and SST equations in a stationary (*i.e.* absolute) Cartesian coordinate system is:

$$\frac{\partial}{\partial t} \left(\int_{C(t)} \mathbf{U} dC \right) + \oint_{S(t)} (\Phi_c - \Phi_d) \cdot d\mathbf{S} - \int_{C(t)} \mathbf{S}_A dC = 0 \quad (1)$$

where $\mathbf{U} = [\rho \quad \rho \underline{u}^T \quad \rho E \quad \rho k \quad \rho \omega]^T$ is the array of conservative variables, the superscript T denotes the transpose operator, and the symbols ρ , \underline{u} , E , k and ω denote, respectively, density, absolute velocity vector, and the total energy, turbulent kinetic energy and specific dissipation rate of turbulent kinetic energy per unit mass. The total energy is $E = e + (\underline{u} \cdot \underline{u})/2 + k$, where e denotes the internal energy per unit mass; the perfect gas law is used to express the static pressure p as a function of ρ , E ,

k and the mean kinetic energy per unit mass $(\underline{u} \cdot \underline{u})/2$ [18]. The generalized convective flux vector $\underline{\Phi}_c$ is:

$$\underline{\Phi}_c = \begin{bmatrix} \rho(\underline{u} - \underline{u}_b)^T \\ \rho(\underline{u} - \underline{u}_b)^T \underline{u} + pI \\ \rho E(\underline{u} - \underline{u}_b)^T + p\underline{u}^T \\ \rho k(\underline{u} - \underline{u}_b)^T \\ \rho \omega(\underline{u} - \underline{u}_b)^T \end{bmatrix} \quad (2)$$

where I is the (3×3) identity matrix, and \underline{u}_b is the boundary velocity.

The definition of the generalized diffusive flux vector $\underline{\Phi}_d$ is reported in [18, 19], and the source term \mathbf{S}_A is given by:

$$\mathbf{S}_A = [0 \quad \underline{0}^T \quad 0 \quad S_k \quad S_\omega]^T \quad (3)$$

where S_k and S_ω denote respectively the source terms of the k and ω equations of the SST turbulence model [20].

In many applications involving rotational motion, such as turbomachinery, helicopter and HAWT rotor flows, it is convenient to formulate the governing equations in a rotating (*i.e.* relative) frame of reference. In simple cases, such as the aerodynamic analysis of fixed-bottom HAWT rotors in uniform wind parallel to the rotor axis, this enables solving a problem that is unsteady in the stationary frame as a steady problem in the rotating frame.

Solving the governing equations in the relative frame, the grid is always motionless during the simulation. However, the relative flow velocity vector can be expressed either in the relative or the absolute frame [21]. The two choices are mathematically equivalent, but representing the relative fluid velocity in the absolute frame is numerically more convenient for open rotor applications. Using an absolute frame representation of the relative fluid velocity, the counterpart of System (1) in a rotating Cartesian frame is:

$$\frac{\partial}{\partial t} \left(\int_C \mathbf{U} dC \right) + \oint_S (\underline{\Phi}_c - \underline{\Phi}_d) \cdot d\underline{S} - \int_C \mathbf{S}_R dC = 0 \quad (4)$$

The expressions of \mathbf{U} , $\underline{\Phi}_c$, and $\underline{\Phi}_d$ in System (4) are identical to those in System (1). However, the control volume C and its boundary S are no longer time-dependent. The source term vector \mathbf{S}_R differs from the source term \mathbf{S}_A because of additional terms due to the inertial forces in the rotating frame, and is given by:

$$\mathbf{S}_R = [0 \quad \rho(\underline{\Omega}_r \times \underline{u})^T \quad 0 \quad S_k \quad S_\omega]^T \quad (5)$$

where $\underline{\Omega}_r$ denotes the angular speed of the rotating frame attached to the rotor.

It is noted that the source term depending on $\underline{\Omega}_r$ in Eq. (5) and the face velocities of the grid cells \underline{u}_b in Eq. (2) are nonzero also for steady rotor flows.

3 GRID VELOCITIES

When the control volume C in Systems (4) and (1) represents one cell of the rotating grid attached to a fixed-bottom HAWT rotor, \underline{u}_b is given by:

$$\underline{u}_b = \underline{\Omega}_r \times \underline{r} \quad (6)$$

in which \underline{r} denotes the time-dependent position vector in the absolute frame with respect to a point on the rotational axis, and $\underline{\Omega}_r$ is the constant angular speed of the rotor.

In this study, the rotational axis of fixed-bottom HAWT rotors is the z axis. To obtain the FOWT rotor grid velocities associated with the concurrent rotation of the rotor past its axis and the pitching motion of the tower past the turbine center of gravity, it is necessary to start from the expressions of the time-dependent grid coordinates in the case of the fixed-bottom turbine. With reference to the schematic of Fig. 1, the time-dependent x - and y -coordinates of a grid point are thus:

$$\begin{aligned} x_r &= x_0 + (x_0 - x_{rot})(c - 1) - (y_0 - y_{rot})s \\ y_r &= y_0 + (x_0 - x_{rot})s + (y_0 - y_{rot})(c - 1) \end{aligned} \quad (7)$$

where x_{rot} and y_{rot} are respectively the x - and y -coordinates of a point on the rotational axis, x_0 and y_0 are respectively the x - and y -coordinates of a grid point at time $t = 0$, $c = \cos\theta_r$, $s = \sin\theta_r$, and $\theta_r = \Omega_r t$ is the azimuthal position of a reference blade (blade B1 in the right plot of Fig. 1). The time-dependent x - and y - components of the grid point velocity are obtained by taking the time-derivative of the two components of Eq. (7), and are:

$$\begin{aligned} \dot{x}_r &= [-(x_0 - x_{rot})s - (y_0 - y_{rot})c] \Omega_r \\ \dot{y}_r &= [(x_0 - x_{rot})c - (y_0 - y_{rot})s] \Omega_r \end{aligned} \quad (8)$$

The two components of Eq. (8) can be viewed as the scalar counterparts of Eq. (6).

In the case of the rotor of a pitching FOWT oscillating in the yz plane with amplitude Θ_p and angular frequency Ω_p past a pitching center of coordinates (y_p, z_p) , additional terms need to be included in Eq. (7) which provides the time-dependent coordinates of the grid nodes of a fixed-bottom HAWT rotor simulation. With reference to the FOWT schematic of Fig. 2,

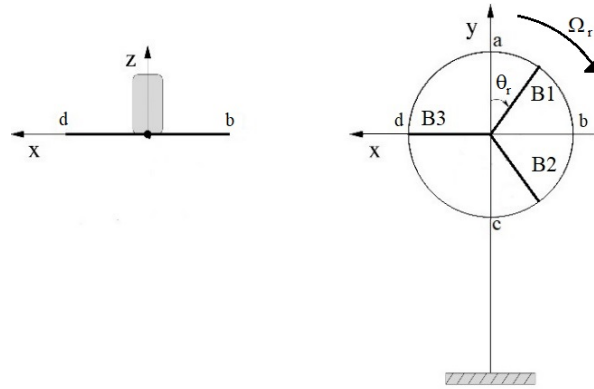


Fig. 1. Top view (left schematic) and front view (right schematic) of fixed-bottom HAWT with axis and rotation conventions.

the time-dependent inclination of the tower is:

$$\theta_p = \Theta_p \sin(\Omega_p t + \phi_p) \quad (9)$$

with ϕ_p being a given phase angle between the instantaneous tower pitch angle θ_p and the rotor azimuthal position θ_r . The expressions of the coordinates of a moving grid point become:

$$\begin{aligned} x &= x_r \\ y &= y_r - (z_r - z_p)s_p + (y_r - y_p)(c_p - 1) \\ z &= z_r + (z_r - z_p)(c_p - 1) + (y_r - y_p)s_p \end{aligned} \quad (10)$$

where $c_p = \cos \theta_p$ and $s_p = \sin \theta_p$. Finally, the grid velocity components associated with concurrent rotation of the rotor and pitching of the tower, obtained by taking the time-derivative of the three components of Eq. (10), are found to be:

$$\begin{aligned} \dot{x} &= \dot{x}_r \\ \dot{y} &= \dot{\theta}_p [-(z_r - z_p)c_p - (y_r - y_p)s_p] + \dot{y}_r c_p \\ \dot{z} &= \dot{\theta}_p [-(z_r - z_p)s_p + (y_r - y_c)c_p] + \dot{y}_r s_p \end{aligned} \quad (11)$$

where $\dot{\theta}_p = \Theta_p \Omega_p \cos(\Omega_p t + \phi_p)$.

At each physical time of the COSA FOWT rotor simulations presented in this study, the grid displacements and velocities are computed with Equations (10) and (11) respectively. In the FLUENT FOWT simulations, the grid velocities at each time are obtained using a newly developed user-defined function (UDF), in which the entrainment velocities are determined using the expressions of Eq. (11), and the grid displacements are evaluated by numerical integration of the analytical expressions

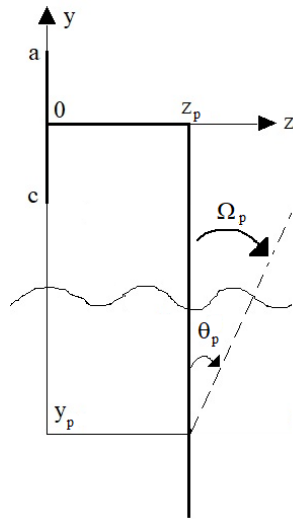


Fig. 2. Side view of FOWT with axis and rotation conventions.

of the grid velocities.

4 COMPRESSIBLE CFD SOLVER

4.1 Space discretization and numerical integration

The compressible density-based COSA code is a finite volume cell-centered code that solves the steady and unsteady time-domain RANS and SST equations using structured multi-block grids [18]. The code has been successfully used to investigate the unsteady hydrodynamics of oscillating wings to extract energy from an oncoming fluid stream [18, 22, 23], the unsteady aerodynamics of Darrieus vertical axis wind turbines [24–26] and the unsteady aerodynamics of fixed-bottom HAWTs due to yawed wind [6, 20] and blade stall [27]. Thorough verification and experimental measurement-based validation studies of the predictive capabilities of COSA for steady and unsteady HAWT rotor flows are reported in references [6, 16, 27]. The code also features an efficient harmonic balance solver for the rapid solution of wind turbine unsteady periodic flows, which has been shown to reduce by up to 50 times the runtime for the NS CFD analysis of fixed-bottom HAWT rotors with respect to the conventional time-domain NS method [6, 19, 28]. COSA has a highly efficient parallelization of both its computing and IO sections [29], and distributed-memory (MPI) simulations have been efficiently run with up to 16,000 cluster cores [25].

The COSA discretization of the convective fluxes of both RANS and SST PDEs uses Van Leer's second order upwind MUSCL extrapolations and Roe's flux-difference splitting with Van Albada's flux limiter. Denoting by \underline{n} the outward normal of the face of a grid cell, and dS the area of said face, the numerical approximation to the continuous convective flux component $\Phi_{cf} = (\underline{\Phi}_c \cdot \underline{n})dS$ through the face is:

$$\Phi_{cf}^* = \frac{1}{2} \left[\Phi_{cf}(\mathbf{U}_L) + \Phi_{cf}(\mathbf{U}_R) - \left| \frac{\partial \Phi_{cf}}{\partial \mathbf{U}} \right| \delta \mathbf{U} \right] \quad (12)$$

The superscript $*$, the subscript f , and the subscripts L and R denote numerical approximation, face value, and value extrapolated from left and the right of the face, respectively. The numerical dissipation is the third term in the right-hand-side of Eq. (12), and is thus seen to depend on the generalized flux Jacobian $\partial\Phi_{cf}/\partial\mathbf{U}$ and the flow state discontinuity across each cell face, defined by $\delta\mathbf{U} = (\mathbf{U}_R - \mathbf{U}_L)$. It can be shown that the seven components of abovesaid numerical dissipation depend on the absolute value of the three distinct eigenvalues of $\partial\Phi_{cf}/\partial\mathbf{U}$, which are given by

$$\lambda_1 = u_n - u_{bn}, \quad \lambda_{2,3} = u_n - u_{bn} \pm a \quad (13)$$

where $u_n - u_{bn} = (\underline{\mathbf{u}} - \underline{\mathbf{u}}_b) \cdot \underline{\mathbf{n}}$ and a is the sound speed. The convective eigenvalue λ_1 has multiplicity 5, whereas both acoustic eigenvalues λ_2 and λ_3 have multiplicity 1. In the COSA simulations presented below, the absolute value of all three eigenvalues have been subjected to the cut-off condition:

$$|\lambda| = \max(|\lambda|, \delta) \quad (14)$$

where δ is a constant equal to 0.76 times the Mach number of the freestream absolute wind speed. The components of the numerical dissipation depend linearly on the abovesaid eigenvalues, and the cut-off condition of Eq. (14) was used to prevent the numerical dissipation from vanishing where one or more of the eigenvalues tend to zero. It is also noted that COSA solves a nondimensionalized form of the conservation laws, in which the flow velocities become the associated Mach number.

The discretization of the diffusive fluxes and the turbulent source terms uses central finite-differencing. The integration of the steady RANS and SST equations is performed in a strongly-coupled fashion [18], using an explicit method made up of explicit Runge-Kutta time-marching, with local time-stepping, implicit residual smoothing and multigrid for convergence acceleration. The strongly-coupled integration approach results in the RANS and SST equations being solved with the same numerical method and being time-marched concurrently. TD problems are solved using Jameson's second-order dual time-stepping. Further detail of the space-discretization and the numerical integration of steady and general time-dependent problems can be found in [18].

4.2 Low-speed preconditioning

The solution accuracy of density-based CFD codes decreases in the presence of low-speed flow regions where the local Mach number drops below the threshold of 0.10 [22], and this accuracy loss is particularly severe in the case of separated flows [30]. The primary cause of this phenomenon is the improper scaling of the components of the numerical dissipation as the local Mach number tends to zero. When solving the density-based compressible flow equations using an explicit integration method, low flow speeds may also result in a reduction of the residual convergence rate. In inviscid and, to a significant extent, also in high-Reynolds number flows, this occurs because of the large disparity of acoustic

and convective speeds, whose component normal to a face of a particular grid cell is provided by Eq. (13). Low-speed preconditioning (LSP) [31] can resolve the accuracy issue by restoring the balance of all terms appearing in the matrix-valued numerical dissipation as the Mach number tends to zero (incompressible flow limit), and can improve the convergence rate by substantially reducing the disparity of acoustic and convective speeds. Indeed, the re-equalization of the characteristic speeds yields convergence rates which, for inviscid and relatively simple viscous flow problems, are fairly independent of the Mach number [22]. The COSA LSP algorithm is a generalization of the preconditioner of Weiss and Smith [32]. The unique feature of the LSP algorithm implemented in COSA [33] is that it is applied to both the RANS and SST equations, a feature required for using the computationally efficient strongly coupled integration of the two sets of equations also for problems containing low-speed regions.

The introduction of LSP modifies the numerical dissipation appearing in the numerical flux defined by Eq. (12) as follows:

$$\Phi_{cf}^* = \frac{1}{2} \left[\Phi_{cf}(\mathbf{U}_L) + \Phi_{cf}(\mathbf{U}_R) - \Gamma_c^{-1} \left| \Gamma_c \frac{\partial \Phi_{cf}}{\partial \mathbf{U}} \right| \delta \mathbf{U} \right] \quad (15)$$

The expression of the preconditioning matrices Γ_c and $(\Gamma_c)^{-1}$ are reported in [33], where one finds that both of these matrices depend on a local preconditioning parameter M_p . The value $M_p = 1$ results in both matrices becoming the identity matrix, and, thus, no preconditioning. In low-speed flow analyses, instead, M_p is given by:

$$M_p = \min(\max(M, M_{pg}, M_{vis}, \varepsilon_p), 1) \quad (16)$$

where M is the local Mach number, M_{pg} is a cut-off value based on the local pressure gradient [34], M_{vis} is a viscous cut-off value [22], and ε_p is a constant cut-off value that prevents $(\Gamma_c)^{-1}$ from becoming singular where all other arguments of the \max function in Eq. (16) approach zero. In the COSA simulations discussed below, the constant ε_p was set to 4.6 times the Mach number of the freestream absolute wind speed.

At the algorithmic level, the key alteration of the numerical dissipation induced by LSP manifests itself in an alteration of the acoustic eigenvalues of the preconditioned Jacobian $\Gamma_c \frac{\partial \Phi_{cf}}{\partial \mathbf{U}}$. The preconditioned eigenvalues are:

$$\lambda_1 = u_n - u_{bn}, \quad \lambda_{2,3} = \frac{1}{2}(u_n - u_{bn})(1 + M_p^2) \pm a' \quad (17)$$

with the artificial sound speed a' given by:

$$a' = \sqrt{4a^2M_p^2 + (M_p^2 - 1)^2(u_n - u_{bn})^2} \quad (18)$$

The cut-off defined by Eq. (14) is also applied to the preconditioned eigenvalues defined by Eq. (17).

5 INCOMPRESSIBLE CFD MODEL

The incompressible flow simulations presented herein have been performed using the commercial finite volume CFD code ANSYS FLUENT Release 19.1, which integrates the discretized equations over general unstructured grids. The same grids were used for both COSA and FLUENT simulations. A cell-centered formulation has been used for the analyses reported below, adopting a second-order accurate upwind space-discretization of the RANS and SST equations. In the case of the unsteady simulations associated with the considered FOWT flow field, a first order dual time-stepping time-marching process has been used. The incompressible model makes use of the pressure-based formulation of the RANS equations, and the numerical integration is obtained by resorting to the COUPLED solver; with this integration method, the momentum and the pressure-based continuity equations are solved in a fully-coupled fashion. The SST transport equations are instead integrated in a segregated or loosely coupled fashion. Since, as discussed below, the mesh resolution at the walls is sufficiently high, also in FLUENT the near-wall region of the boundary layer is fully resolved without resorting to wall functions. Similarly to the COSA simulations, the steady rotor flow analyses in FLUENT have been performed in the rotor frame using an absolute frame representation of the unknown flow velocity, whereas the time-dependent FOWT simulations have been carried out in the absolute frame.

6 RESULTS

The study below was performed considering the NREL 5 MW virtual HAWT [35]. The turbine has a tower height of 90 m and features a 126 m-diameter three-blade rotor. The rotor has an overhang of 5 m, a shaft tilt of 5° , and a pre-coning of 2.5° . The rotor pre-coning is not included in the following analyses.

Steady and time-dependent low- and high-fidelity simulations are considered. In all steady analyses, the turbine has a fixed-bottom tower, and the shaft tilt is neglected. The time-dependent analyses are used for analyzing the pitching FOWT rotor unsteady performance and aerodynamics. The same grid and the same numerical set-ups of the steady flow analyses are used for the time-dependent CFD simulation. The shaft tilt is included in both low- and high-fidelity analyses. In the CFD analyses, the shaft tilt is accounted for by inclining the oncoming steady wind by 5° on the horizontal direction, thus allowing one to adopt the same rotor geometry and meshes used for the steady flow analyses.

The rotor geometry and the selected wall boundary conditions are reported in Fig. 3(a), the grid around the airfoil at 50% tip radius is shown in Fig. 3(b), and the physical domain and position of the boundaries are provided in Fig. 3(c). The COSA simulations are performed using characteristic far field boundary conditions, which automatically detect if the flow enters

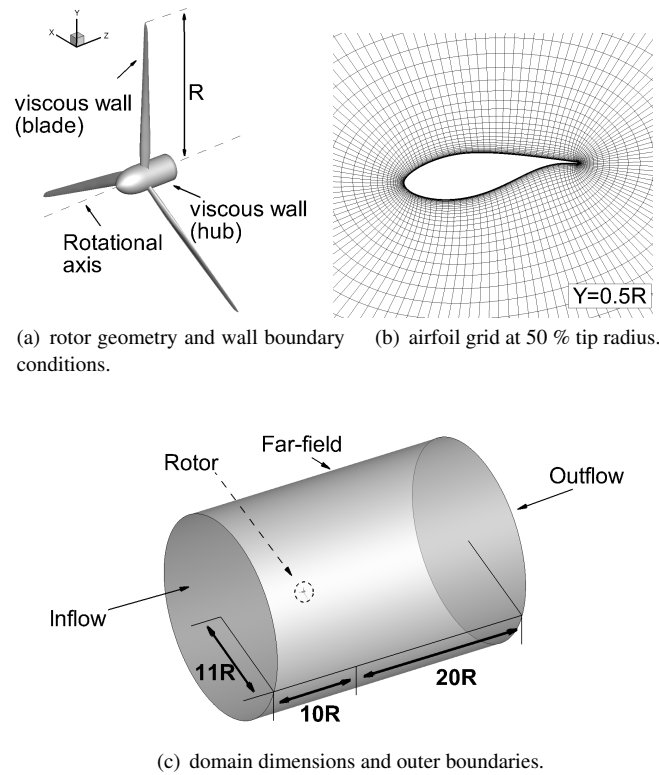


Fig. 3. CFD model of NREL 5 MW turbine.

or leaves the domain, on all far field boundaries. The FLUENT simulations are performed using a velocity inlet condition on the front inflow boundary and the lateral far field boundary, whereas a pressure outlet is enforced on the rear outflow boundary. All CFD simulations assume fully turbulent boundary layers at solid wall boundaries. This choice is made not only to avoid the additional computational burden incurred by using a transition model, but also because blade leading edge erosion [36, 37] experienced in just a few years of operation is expected to result in the blade boundary layers being fully turbulent at most operating conditions, also due the high Reynolds number encountered over most parts of the blades.

Two structured multi-block grids with high level of orthogonality in most regions of the domain and differing for their overall refinement are adopted for the CFD simulations. For both grids, the distance of the far field boundaries from the turbine rotor indicated in Fig. 3(c) is set following the guidelines in [38], and a butterfly mesh pattern is used around the rotor axis to avoid the use of degenerate cells with the COSA structured code. The coarser grid has about 10M cells, with minimum distance of the first grid nodes off the blade surface from the blade surface itself yielding y^+ of about 1 in both steady and time-dependent simulations. In comparison to the grid used for the simulations in [16], the present coarser grid has 25% more cells discretizing a physical domain which is eight times smaller. The finer 80M cell mesh, also used for the steady flow analyses discussed below, is obtained from the 10M cell-grid by doubling the number of cells in each direction.

6.1 Fixed-tower rotor analyses

Two operating conditions below rated wind speed are considered for the analysis of fixed-tower rotor aerodynamics: a near-rated condition, with wind speed of 11 m/s and rotational speed of 12 RPM, and an intermediate condition with wind

speed of 8 m/s and rotational speed of 9.16 RPM. The freestream conditions have pressure of 1 bar, temperature of 283 K and density of 1.225 kg/m³.

Tables 1 and 2 reports the COSA, FLUENT and FAST estimates of the rotor power and thrust at 11 m/s and 8 m/s respectively. The FAST results of these two tables are computed with the OpenFAST release of this code [11]. To be as consistent as possible with the CFD analyses, the FAST analyses were run using high-Reynolds number ($> 5 \text{ M}$) airfoil lift and drag data. The quantitative agreement among the results of the two CFD codes and FAST is very good. At the near-rated condition, the FLUENT and COSA coarse grid thrusts are underestimated by 4.8% and 3.7%, respectively, with respect to that of FAST. Increasing the mesh refinement, the CFD and BEMT results get closer, with the FLUENT and COSA thrust underestimates of the FAST prediction reducing to 3.2% and 3.4% respectively. Smaller differences are observed in terms of rotor power: the FLUENT and COSA coarse estimates are respectively 1.8% and 0.6% of the FAST prediction, with these differences changing to 0.2% for both CFD fine grid estimates. At the intermediate wind-speed, the qualitative differences between the high- and low-fidelity results are identical to those at the near-rated condition, and the numerical values of these differences are very close to their near-rated wind speed counterparts. These results indicate that the two CFD codes can be considered equivalent for predicting fixed-bottom HAWT steady performance. Moreover, the coarse grid is seen to possess a level of spatial refinement yielding fairly grid-independent results.

Table 1. Fixed-bottom turbine ($u_\infty=11 \text{ m/s}$, $\Omega_r = 0.4\pi \text{ rad/s}$): rotor thrust T and rotor power P computed with coarse and fine COSA and FLUENT simulations and FAST analysis.

	FAST	COSA-C	FLUENT-C	COSA-F	FLUENT-F
T [N]	703.8	677.8	670.3	679.9	681.0
P [MW]	4.91	4.94	4.82	4.92	4.92

Table 2. Fixed-bottom turbine ($u_\infty=8 \text{ m/s}$, $\Omega_r=0.9592 \text{ rad/s}$): rotor thrust T and rotor power P computed with coarse and fine COSA and FLUENT simulations and FAST analysis.

	FAST	COSA-C	FLUENT-C	COSA-F	FLUENT-F
T [N]	383.9	365.8	364.5	364.1	NA
P [MW]	1.90	1.90	1.86	1.87	NA

The COSA and FLUENT coarse grid profiles of static pressure coefficient c_p of four blade cross-sections for the near-rated condition are depicted in Fig. 4. The pressure coefficient is defined as:

$$c_p = \frac{p_\infty - p}{\frac{1}{2}\rho_\infty [u_\infty^2 + (\Omega r)^2]} \quad (19)$$

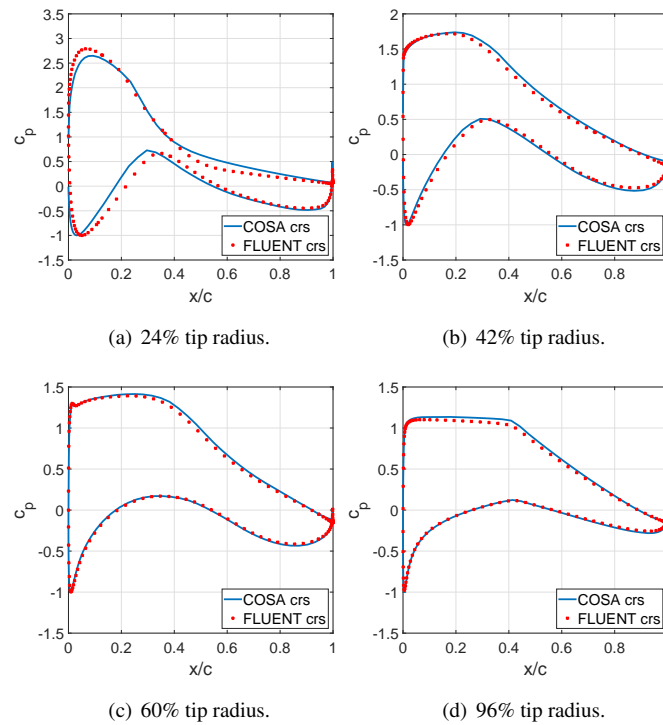


Fig. 4. Fixed-bottom turbine ($u_\infty=11$ m/s, $\Omega_r = 4\pi$ rad/s): COSA and FLUENT coarse grid static pressure coefficient c_p at four radial positions.

where p and p_∞ denote, respectively, local and freestream static pressure, u_∞ is the freestream wind speed and r denotes the radial position along the blade. The COSA and FLUENT c_p profiles of Fig. 4 differ negligibly. The agreement of the two predictions is excellent along most of the blade. Some small differences between the predictions of the two codes exist only at the section closest to the hub, where the two codes predict similar c_p values on the pressure side but a lower pressure level is predicted by COSA, corresponding to higher lift. The fine grid c_p profiles of both codes, not reported for brevity, show that the coarse grid blade static pressure predictions of both analyses are grid-independent.

Figure 5 reports the limiting streamlines on the blade suction side computed by the two CFD simulations using the coarse grid. The plots show overall good qualitative agreement with the limiting streamline plot of [38], which refers to a wind speed of 8 m/s. The qualitative comparison of the results of these two articles is enabled by the fact that the tip speed ratio (TSR) at 8 and 11 m/s are very close. A large separation occurs in the hub region of the blade, whose chordwise and spanwise extent is slightly larger in the COSA simulation. The impact of these differences on the blade performance can be adequately quantified by considering the c_p profiles of Fig. 4. At 24% tip radius, corresponding to a radius of 15.6 m, FLUENT predicts the separation at about 50% of the chord and COSA at about 40% of the chord. However, the top right plot of Fig. 4 shows that at 42% tip radius, corresponding to a radius of 27.2 m, the blade load predicted by the two simulations is much closer, indicating that the differences between the separation highlighted by the limiting streamlines correspond to less dramatic differences in terms of blade load. Outside the separation zone, the limiting streamlines of the two codes are in good quantitative agreement on the rest of the blade surface, particularly in the outboard region, where the majority of the wind energy harvesting occurs. The larger extent of the surface separation predicted by COSA may be due to a suboptimal choice of the LSP parameter ϵ_p , an item of future work.

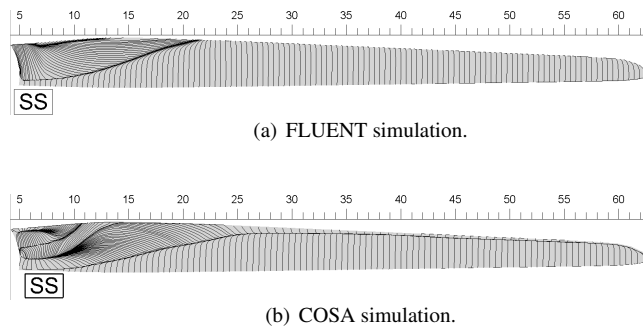


Fig. 5. Fixed-bottom turbine ($u_\infty=11$ m/s, $\Omega_r = 4\pi$ rad/s): FLUENT and COSA coarse grid limiting streamlines on blade suction side (SS).

The results above indicate that the adopted computational set-ups allow performing reliable simulations of rotor aerodynamics, a key requirement for FOWT performance prediction. However, in view of analyzing floating wind farms, the capability of the CFD models of simulating the flow behind the turbine is also important. To highlight the main flow structures in the rotor wake, the azimuthal component of the absolute vorticity ω_θ is considered. Its definition is:

$$\omega_\theta = (\nabla \times \underline{u}) \cdot \underline{e}_\theta \quad (20)$$

where \underline{e}_θ is the circumferential unit vector of the cylindrical system whose z axis coincides with the homonymous axis of the absolute Cartesian system in which the rotor flow is represented. Figure 6 compares the coarse mesh contours of ω_θ in the meridional plane yz . The wake of the rotor is delimited by the blade tip vortices. Dense cores of negative ω_θ appear on the two sides of the meridional plane, alternating due to the helical pattern of the vortex tube. The 3D visualization of the tip vortex streamtube in the right plot of Fig. 6 consists of an ω_θ isosurface colored with the local radius to improve its visibility. The wake vorticity field predicted by the two codes are similar, and the tip vortex is also well resolved, although the FLUENT simulation on this coarse grid appears to be slightly less dissipative than the COSA simulation, since the former resolves for a longer axial distance the helical vorticity streamtubes.

The considered coarse grid has been shown to provide mesh-independent results in terms of rotor loads and power. To investigate the impact of mesh refinement on rotor wake resolution, Fig. 7 visualizes the rotor wake obtained with a fine grid COSA simulation using the same format of Fig. 6. The overall pattern of the vorticity field does not change notably over that of the coarse grid COSA solution. However, the ω_θ cores are resolved more neatly, and the helical vortex patterns are resolved on a longer axial distance. This higher wake resolution further away from the rotor does not affect significantly the rotor loads and the wake generation patterns discussed below. Thus, in light of the good quality of the coarse grid solution of both codes, and the high computational cost of the fine-mesh time-dependent simulations, the coarse mesh was selected for the FOWT analyses below.

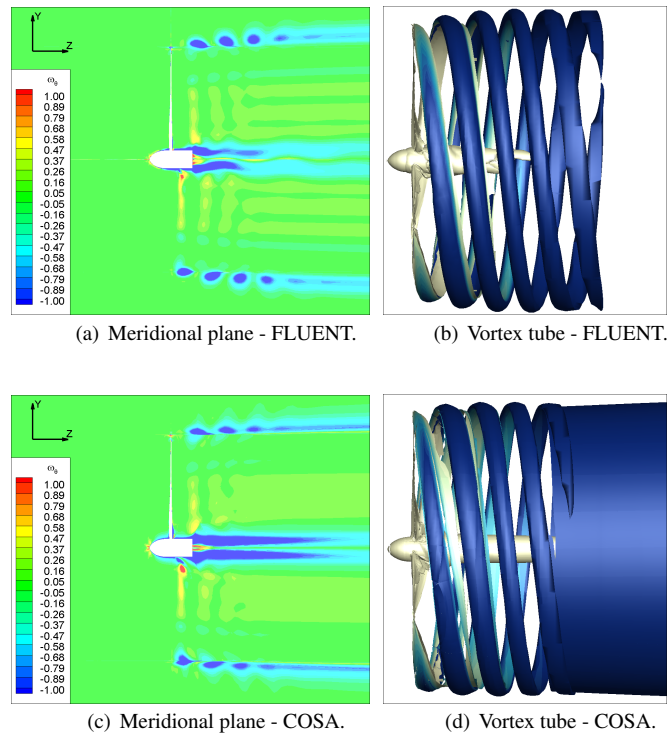


Fig. 6. Fixed-bottom turbine ($u_\infty=11$ m/s, $\Omega_r = 4\pi$ rad/s): COSA and FLUENT coarse grid contours of azimuthal vorticity ω_θ [1/s] in meridional (yz) plane (left) and ω_θ streamtubes behind rotor (right).

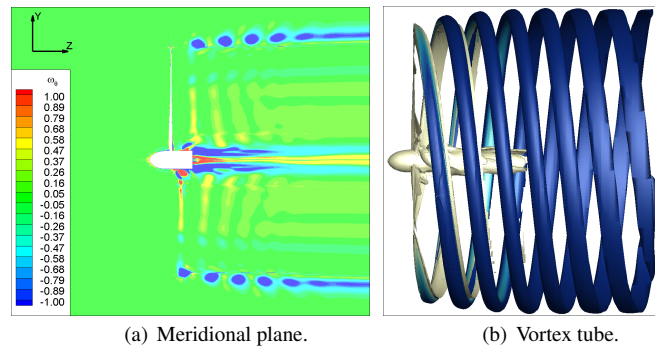


Fig. 7. Fixed-bottom turbine ($u_\infty=11$ m/s, $\Omega_r = 4\pi$ rad/s): COSA fine grid contours of azimuthal vorticity ω_θ [1/s] in meridional (yz) plane (left) and ω_θ streamtubes behind rotor (right).

6.2 Pitching FOWT rotor analyses

The pitching FOWT analysis is performed for the near-rated operating regime only, corresponding to freestream wind speed of 11 m/s and rotor speed of 12 RPM. The rigid body pitching motion is imposed to the whole rotor (hub and blades) with amplitude $\Theta_p = 4^\circ$ and angular frequency $\Omega_p = 0.4\pi$ rad/s, which equals the angular frequency of the rotor speed. The simulations do not include blade pitch and rotor speed control, and the motivation of this choice and its impact on the analyses are discussed below. The phase ϕ_p between the pitching motion and the rotor revolution is set to zero. This implies that, at the beginning of the pitching cycle the turbine tower is vertical and has maximum leeward (*i.e.* in positive z direction) speed, and blade 1 in Fig. 1 is vertical above the hub. At 50% of the pitching cycle the tower is again vertical but it has maximum windward speed, and blade 1 is vertical below the hub. The pitching center is at the tower base at $y_p=-90$

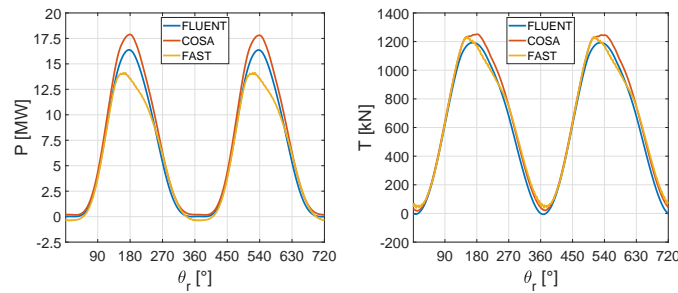


Fig. 8. Pitching FOWT ($u_\infty=11$ m/s, $\Omega_r = \Omega_p = 0.4\pi$ rad/s, $\phi_p = 0^\circ$, $\Theta_p = 4^\circ$, $y_p=-90$ m, $z_p=5$ m): FLUENT, COSA, and FAST rotor power (left) and rotor thrust (right) over two consecutive periods.

m, and the rotor overhang is accounted for by placing the pitching center at $z_p=5$ m. Both the COSA and FLUENT analyses are carried out in the absolute reference frame. The selected frequency of the turbine motion, which is one of the regimes analyzed in [8], results in a maximum axial acceleration of the turbine nacelle of about 9.9 m/s², a value above the threshold of $0.2g$ to $0.3g$ at which the turbine safety system would shut down the machine [39]. Therefore, the selected kinematic conditions should be viewed as an extreme operating condition, such as that occurring due to faults of the safety system. It is important to test and assess FOWT aerodynamic analysis codes for extreme conditions, as these often pose design-driving constraints.

Figure 8 compares the periodic profiles of rotor thrust and power of the new CFD analyses of the present study, and those of the FAST simulation of [16]. At each physical time, the rotor thrust is computed as the sum of the projection on the z axis of the aerodynamic force acting on each blade, and this latter results from integrating the pressure and viscous forces on the entire blade surface. This method yields exact estimates at 0% and 50% of the cycle, when the tower is vertical ($\theta_p = 0$), and is affected by a small error ($< 1\%$) at all other times, due to the inclination of the rotor axis caused by the pitching motion. Similarly, the rotor torque is computed as the sum of the aerodynamic moment of each blade past an axis parallel to z and passing through the time-dependent rotor center, and each moment is obtained by integrating on the entire blade surface the moment of the pressure and viscous forces about this axis. The error affecting these torque estimates is qualitatively and quantitatively similar to the thrust error. All curves of Fig. 8 show quasi-harmonic large-amplitude oscillations of rotor thrust and power. These oscillations arise because the analyses do not include blade pitch and rotor speed control, and this also causes the peak rotor power and thrust to significantly exceed their rated values. In real operations, the turbine control greatly reduces these oscillations, or shuts down the turbine when appropriate. One of the aims of the study, however, was to cross-compare the predictive capabilities of FOWT CFD and BEMT codes in severe aerodynamic regimes, an important step which typically precedes the use of these aerodynamic codes for the design and verification of FOWT rotor control.

Both thrust and power achieve their minima around 0% of the cycle, when the tower has maximum leeward speed, and their maxima around 50% of the cycle, when the tower has maximum windward speed. This occurs because at 0% and 50% of the pitching cycle the speed of the rotor hub is maximum and has a magnitude of 7.89 m/s, which is comparable to magnitude of the absolute wind speed of 11 m/s. Therefore, when the turbine has maximum leeward speed, the relative (*i.e.* effective) axial velocity of the wind at hub height is only 3.11 m/s, resulting in all analyses predicting output power below 1 MW. This low value is due both to the lower level of available wind energy, which depends on the cube of the relative

axial wind speed over the rotor swept area, and also the fact that the instantaneous TSR has increased significantly over the optimal value of the steady near-rated operating condition. The latter one is 7.42, a value at which the power coefficient C_p is about 0.46, whereas the instantaneous TSR at 0% of the pitching cycle is 26.26, a value at which notably lower C_p values are observed. When the rotor hub achieves its maximum windward speed at 50% of the pitching cycle, the relative axial velocity of the wind at hub height is 18.89 m/s, resulting in all analyses predicting output power well above the rated value. From a merely aerodynamic viewpoint, these high power peaks are consistent with an effective wind speed of 18.89 m/s. For instance, the peak of 17.6 MW predicted by COSA for this rotor geometry and instantaneous operating condition would correspond to a power coefficient of about 0.33, a realistic value for the instantaneous TSR value of 4.32 at this point of the pitching cycle.

The thrust and power oscillation patterns of the two CFD codes are similar, and are also fairly similar to those of FAST. The peak values of the rotor thrust predicted by the three analyses are in fairly good agreement, although some differences in the slope of the three curves are visible. More notable differences exist among the peak power values of the three analyses: COSA predicts a peak power of 17.6 MW, the FLUENT prediction of 16.4 MW is 7% lower, and the FAST prediction of 14.1 MW is 20% lower. The mean power predicted by the two CFD codes over one cycle, 6.4 MW for FLUENT and 7.1 MW for COSA, is 30 to 45% higher than that predicted by these codes in the fixed-tower simulations. The COSA mean power increase is of the same order of magnitude of those observed for similar compressible flow CFD analyses of a 10 MW FOWT pitching with amplitudes between 3° and 5° [14]. As discussed below, part of the reason for the discrepancies of the power predictions is the existence of compressible flow effects not included in the FLUENT and FAST simulations. But an additional major factor accounting for the large differences between the CFD and BEMT results is likely to be a different prediction of the two methods of the dynamic stall characteristics of pitching and rotating blades. It is also noted that, in a cross-comparative COSA/FAST analysis of FOWT rotor aerodynamic loads in non-extreme pitching regimes [40], the differences between the COSA and FAST predictions have been found to be notably smaller than those for the extreme condition considered herein.

To investigate in greater detail the unsteady aerodynamics of the considered pitching FOWT rotor, the c_p profiles of four cross-sections of blade 1 at four times of the pitching cycle presented in Fig. 9 are considered. The left and right plots report the COSA and FLUENT profiles, respectively. Each plot reports the c_p profiles at 0% and 50% of the cycle, the instants at which the rotor power and thrust take their minimum and maximum values, respectively. To enable a qualitative comparison with the fixed-tower turbine case, the plots also provide the c_p profiles of this reference condition. The c_p profiles of each plot highlight large variations of blade aerodynamics during the pitching cycle, as expected. At 50% of the period (peak power and thrust) the pressure profiles of the three outermost sections resemble those observed in fixed-tower mode, even though the pressure difference between the two sides of the blade is higher, especially in the leading edge region. This is due to higher AoA to the blade with respect to the steady condition. At this point of the cycle, in fact, blade 1, which is vertical below the hub, experiences windward entrainment velocities due to the pitching motion. At the same instant, the other two blades have higher elevation, thus undergoing an even larger increment of aerodynamic loading. The top plots of Fig. 9 show qualitative differences between the steady and FOWT pressure profiles at 50% of the cycle, and this is because in FOWT

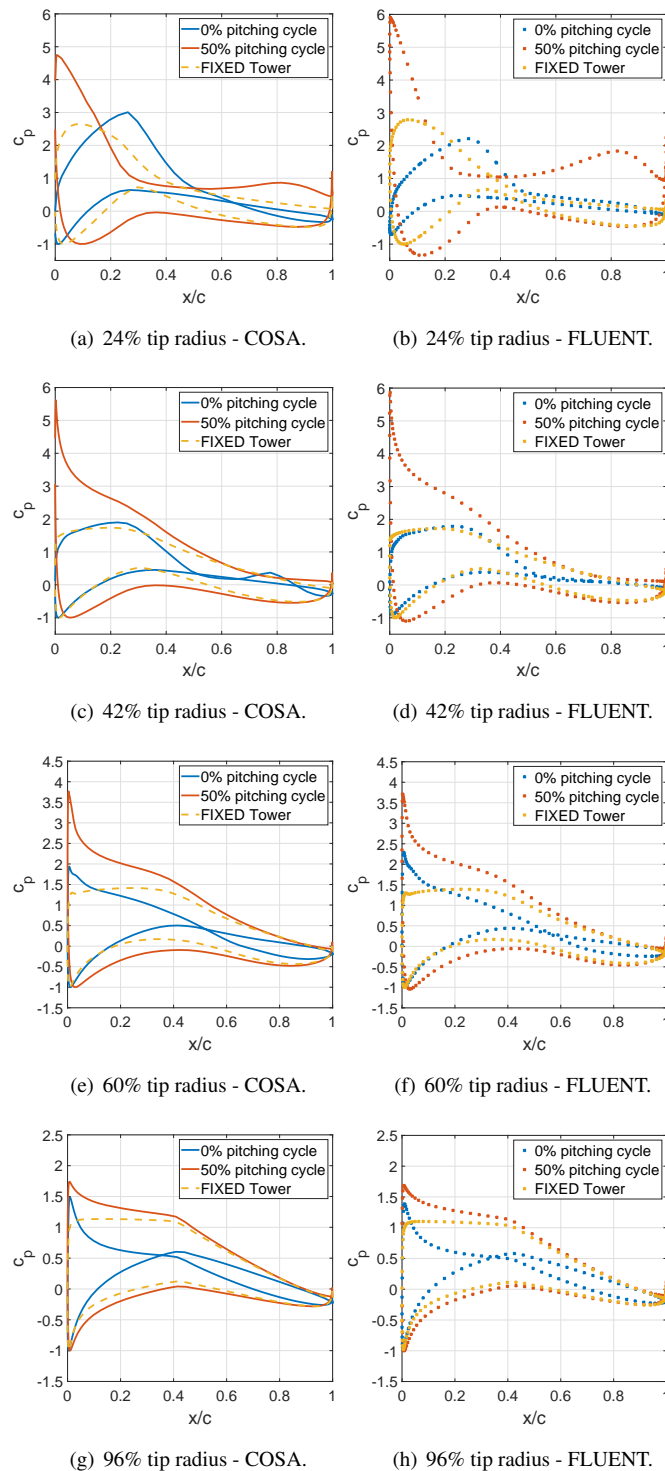


Fig. 9. Static pressure coefficient c_p at four radial positions of blade 1 of pitching FOWT (0% and 50% of pitching cycle) and fixed-bottom turbine computed by COSA (left) and FLUENT (right).

mode the flow separation at the lower blade radii becomes even larger than in the fixed-tower case, due to the blade AoA reaching very high levels. At the beginning of the pitching cycle, the FOWT pressure profiles on the two sides of the blade are much closer to each other, and they even intersect. This is consistent with the substantial AoA reduction caused by low wind speeds relative to the pitching tower in this phase. The two CFD codes provide very similar predictions over most parts of the blade, with some more notable differences appearing only at the hub section. These differences are similar to those

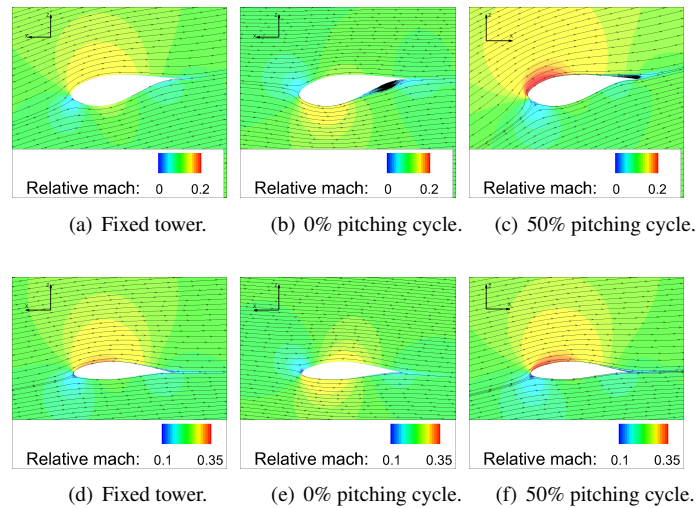


Fig. 10. COSA coarse grid contours of relative Mach number and streamlines at 42% tip radius (top) and 96% tip radius (bottom) of blade 1 of fixed-bottom turbine (left), FOWT at 0% of pitching cycle (center) and FOWT at 50% of pitching cycle.

observed and discussed in the case of the fixed-tower rotor, and they are too limited to justify the differences of peak power predicted by the COSA and FLUENT simulations. The smaller COSA and FLUENT c_p differences at high radii are partly due to compressibility effects, as shown below.

To further investigate the unsteady aerodynamics of the considered FOWT regime and highlight the key differences with fixed-tower rotor aerodynamics, the contours of relative Mach number and the streamlines past the cross-sections of blade 1 at 42% and 96% tip radius for the fixed-bottom turbine and the pitching FOWT case are reported in Fig. 10. The left plots refer to the blade sections of the fixed-bottom turbine, and the middle and right plots refer to the two sections at 0% and 50% of the pitching cycle. Cross-comparison of the six plots highlights flow features in line with the key findings of the c_p profile analyses based on the results in Fig. 9, more specifically: (i) the qualitative similarity of the steady pressure field and that of the pitching rotor blade at 50% of the pitching cycle, (ii) the significant load increase of the pitching blade with respect to the steady case, due to the higher AoA caused by the windward motion of the tower and resulting in flow separation at the inboard part of the blade in the trailing edge region, and (iii) the inversion of pressure and suction side in the pitching regime at the beginning of the pitching cycle. The Mach contour plot past the outer section at 50% of the pitching cycle also indicates Mach numbers well in excess of 0.3. Indeed, it is found that a significant portion of the outer part of the blade has peak Mach numbers in the suction side region well above 0.4 in this phase of the tower motion. This results in compressible flow effects that cannot be captured by the incompressible flow simulation, as highlighted by the verification provided below.

Inspection of the COSA and FLUENT c_p profile of the blade tip section depicted in Fig. 11 reveals that flow compressibility alters the pressure field with respect to the incompressible solution, an effect that can be quantified. One notes that COSA predicts a slightly lower pressure than FLUENT on the blade suction side. This difference is entirely due to flow compressibility, and this can be proved by correcting the FLUENT pressure profile by means of the so-called Glauert's

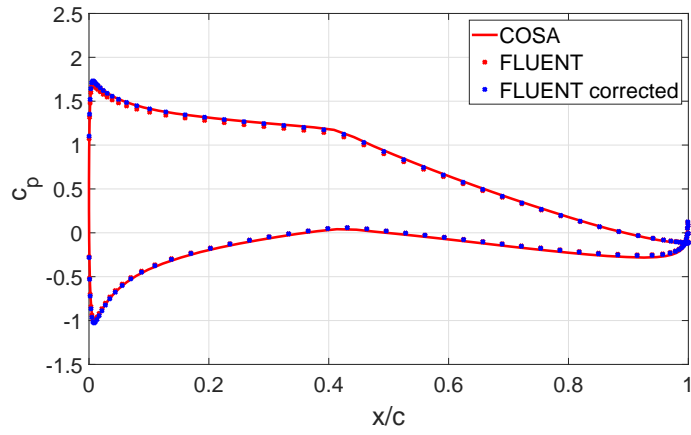


Fig. 11. COSA, FLUENT and Glauert-corrected profiles of static pressure coefficient c_p at 96% tip radius at 50% of pitching cycle.

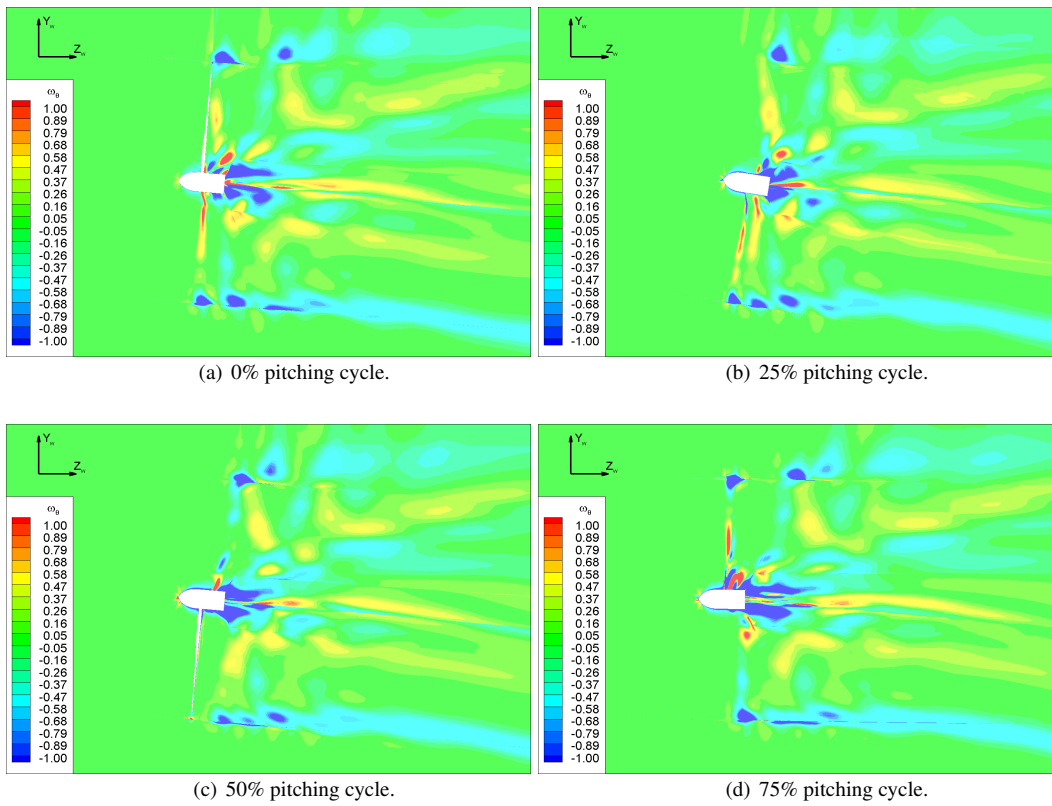


Fig. 12. COSA coarse grid contours of azimuthal vorticity ω_θ [1/s] in yz plane at 0%, 25%, 50% and 75% of pitching cycle.

transformation rule [41]:

$$c_{p,corr} = \frac{c_p}{\sqrt{1 - M_w^2}} \quad (21)$$

Using the relative Mach number of the approaching wind, $M_w = 0.23$, the corrected pressure profile matches exactly the COSA prediction, as seen in Fig. 11. The aforementioned verification was performed by computing M_w ignoring the induction effect. However, the relative velocity is dominated by the entrainment velocity of the rotor; as a result, the impact of

the induction on the M_w estimate is not expected to be significant. Indeed, whether neglecting the induction or using the induction factor estimated by FAST, the M_w estimates vary by less than 1%. Neglecting flow compressibility reduces slightly the lift generated by the tip sections, thus implying a slight underestimate of the turbine power in the FLUENT simulation. Applying Glauert's correction to the entire surface of the three blades, and integrating the resulting static pressure to obtain the overall rotor power, the peak power of the FLUENT simulation increases by about 2.5%, thus reducing the difference between the peak power of COSA and FLUENT to less than 5%.

The CFD FOWT results above highlighted high levels of rotor flow unsteadiness, likely to alter the wake generation process and the wake/rotor interaction losses of floating wind farms with respect to the fixed-bottom turbine case. As the fixed-tower rotor analyses showed that both codes deliver good and comparable wake resolution, only COSA simulations are used below to analyze FOWT wake physics. Contour plots of the azimuthal component ω_θ of the absolute vorticity at 0%, 25%, 50% and 75% of the pitching cycle are provided in the four plots of Fig. 12. The wind is directed along the positive z_w axis. In the simulations, the rotor tilt was accounted for by pitching the wind at the far field boundaries by the tilt angle of 5° on the z axis rather than tilting the rotor in the grid. The $y_w z_w$ reference frame of Fig. 12 is rotated by 5° in the clockwise direction with respect to the original z axis. Thus, the tower axis at 0% and 50% of the pitching cycle is parallel to y_w . In all cases, ω_θ refers to the cylindrical system with axis z . Comparing the four plots of Fig. 12 to their fixed-tower rotor counterparts in Fig. 6, notable differences of the tip vortex pattern are observed. More specifically, the FOWT tip vortices lose the coherent circular cross-section pattern observed in steady conditions. Moreover, significant differences appear between the upper and lower regions of the FOWT wake, the latter appearing more similar to its fixed-tower counterpart. This is due to the fact that the velocity perturbation associated with the pitching motion is lower at lower radii. The top region of the wake exhibits the highest differences with respect to the fixed-tower case, and also a significant dependence on time. Two fairly distant tip vortex cores are visible at the beginning of the cycle, which evolve in a single core at 25% of the period, when the rotor reaches its furthest downstream position. When the turbine reaches maximum windward speed (50% of pitching cycle), two relatively close vortex cores appear. At 75% of the period, these two vortex cores have moved downstream of the rotor maintaining their initial axial spacing and a third vortex core next to the rotor tip appears. It is noted however, that the axial distance between this new third core and the following one is notably larger than that between the two cores at 50% of the pitching cycle. These phenomena highlight a complex pattern of the generation and near-field propagation of tip vortex in the upper region of the rotor wake, investigated below in greater detail.

During the pitching cycle, the rotor undergoes significant variations of the blade AoA, whose minimum values yield nearly zero blade lift around the initial part of the considered cycle. As lift is the main driving force of the tip vortex, the generation strength of the latter also experiences a periodic cycle, resulting in an intermittent release of tip vortices in the upper region of the rotor wake. It is also noted that the axial spacing of the ω_θ tip vortex helical streamtubes of the floating rotor varies during the oscillation cycle. Moreover, in the considered case of pitching motion, unlike the surging rotor case, this axial spacing varies also azimuthally at all times, due to the linear dependence of the tower-induced velocity on the distance from the pitching center, *i.e.* the elevation y . These phenomena are further analyzed in Fig. 13, reporting the ω_θ contours of the fixed-tower rotor flow field, and the pitching FOWT rotor flow fields at 0% and 50% of the pitching cycle

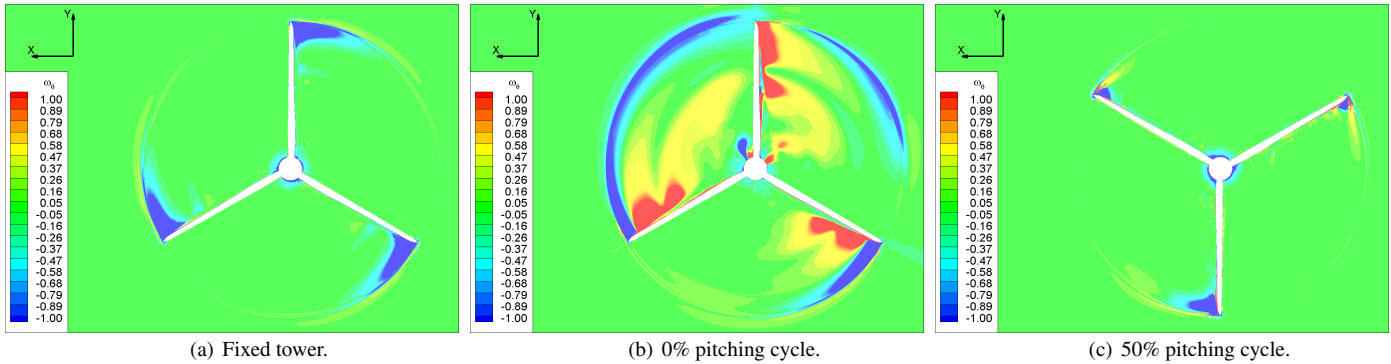


Fig. 13. COSA coarse grid contours of azimuthal vorticity ω_θ [1/s] in xy plane of fixed-bottom turbine (left), FOWT at 0% of pitching cycle (center) and FOWT at 50% of pitching cycle (right).

in the xy plane, which contains the rotor center. When the pitching FOWT rotor moves windward (plot at 50% cycle), the footprint of the tip vortices is notably smaller than in the fixed-tower case. This is because the relative axial velocity of the wind is maximum, resulting in the constant- ω_θ helices moving rapidly downstream of the rotor and their axial spacing also being maximum in the cycle. However, as the strength of this phenomenon increases with the elevation y, this effect is minimum for the blade tip at the lowest y coordinate, which indeed shows the largest tip vortex footprint of the pitching rotor blades, and the axial spacing of the helices is minimum at this elevation. The footprint of the tip vortices is more pronounced at the beginning of the period (plot at 0% cycle), when the rotor has maximum leeward speed. In these conditions, the relative axial velocity of the wind reaches its minimum levels and even becomes negative at the highest y values. The high entrainment speed in the leeward direction reduces the axial spacing of the constant ω_θ helices, and therefore the xy plane intersects an azimuthally longer portion of these vorticity streamtubes.

The ω_θ contour plot at 0% of the pitching cycle of Fig. 13 also explains the intermittent release of tip vorticity in the top part of the rotor, observed in the discussion of Fig. 12. The pressure/suction side inversion of the highest blade, due to the near-zero value of the axial component of the relative wind speed in the tip region, results in near-zero lift forces. This removes the driving force of the tip vortex, which is absent at the tip of this blade, as visible in the middle plot of Fig. 13.

7 CONCLUSIONS

This study presented thorough comparative analyses of pitching FOWT rotor aerodynamics carried out with the BEMT-based FAST wind turbine code, and blade-resolved NS CFD simulations. These latter were performed with the COSA compressible code and the FLUENT incompressible code, in which a new UDF for prescribing FOWT rotor kinematics was developed. The NREL 5 MW HAWT was the selected baseline turbine. A very good agreement of the FAST, compressible and incompressible CFD predictions of the fixed-tower rotor performance at 8 and 11 m/s was observed. This confirms the suitability of the low-fidelity BEMT approach for the analysis of fixed-bottom HAWTs, and also the negligible impact of flow compressibility on the aerodynamics of this utility-scale turbine. The latter finding was also supported by the excellent agreement of the blade surface static pressure distributions and the wake patterns computed with the two CFD analyses.

For an extreme pitching regime, featuring amplitude of 4° and pitching frequency equal to the frequency of the rotor

angular speed, the low- and high-fidelity predictions of the peak rotor thrust of the pitching rotor at the near-rated wind speed of 11 m/s were found to be in relatively close agreement. However, notably larger differences were noted for the peak rotor power. The compressible flow analysis predicted a peak power of 17.6 MW, the incompressible analysis prediction was 7% lower, and the BEMT prediction was 20% lower. The difference between the incompressible and compressible predictions was reduced to less than 5% by applying Glauert's compressibility correction to the incompressible estimate of the blade static pressure at peak rotor power. This confirms that compressibility effects in FOWT rotor flows may be significant and have to be systematically accounted for. The fairly large differences between the BEMT and blade-resolved CFD analyses are likely to be due to different predictions of the dynamic stall affecting rotating blades subjected to time- and space-dependent periodic AoA variations. The stall models of BEMT codes are not validated for this motion type, and significant progress of all FOWT aerodynamic methods could be enhanced by the availability of realistic measured data for code validation. For non-extreme pitching regimes, however, the differences between the time-dependent profiles of turbine power, rotor thrust and blade pitching moments have been found to be notably smaller than in the extreme conditions considered herein [40].

The CFD analyses of the FOWT rotor wake highlighted and discussed the intermittency of FOWT rotor tip vortex and wake generation, caused by the large periodic variations of the tower-induced entrainment velocity and the blade AoA. The lowest values of this variable yield periodic weakening or even interruption of the tip vortex and wake generation in the higher region of the rotor swept area. This phenomenon is common also to surging FOWTs, but the pitching platform case differs from the surging platform case in that the blades of a pitching rotor will have an elevation-dependent (and thus azimuthal position-dependent) and out-of-phase variation of the lift along the blade length. All this results in larger circumferential non-uniformities of pitching rotor wakes, and may lead to a dependence of the wake recovery rate on the FOWT platform type, a key aspect for the design of future FOWT farms.

The COSA code can be used also for the analysis of surging FOWTs, and this kinematic functionality was recently tested in the ARCTIC code, the recently developed incompressible counterpart of COSA [42]. The surging functionality will be used to carry out comparative analysis of wake aerodynamics of fixed-bottom, pitching, and surging FOWTs in future studies. The assessment of compressibility effects in FOWT rotor aerodynamics could be made even more rigorous by using the same baseline code. Future work will include doing this using the compressible COSA code and its recently completed incompressible counterpart, the ARCTIC code. Both codes have a very high parallel efficiency, tested with up to 32,000-core MPI simulations. Moreover, both codes also feature a nonlinear harmonic balance solver for the rapid and accurate solution of periodic open rotor flows, including FOWT rotor flows [40]. These features, along with license-free usage of these codes, make them suitable for very large realistic FOWT analyses.

Acknowledgements

This project was supported by the UK Engineering and Physical Sciences Research Council under Grant EP/T004274/1. The computational work was performed under the Project HPC-EUROPA3 (INFRAIA-2016-1-730897), with the support of the EC Research Innovation Action under the H2020 Programme; Dr. Campobasso acknowledges the support of the Dipar-

timento di Energia - Politecnico di Milano, and the computer resources and technical support provided by the CINECA HPC centre, and Lancaster University for the use of the HEC cluster for part of the COSA simulations. The cross-departmental laboratory CFDHub of Politecnico di Milano is also acknowledged for providing the computational resources for the FLU-ENT simulations. The computational work also used resources from the Fulham HPE Apollo 70 system, supplied to EPCC as part of the Catalyst UK programme, a collaboration with Hewlett Packard Enterprise, Arm and SUSE to accelerate the adoption of Arm based supercomputer applications in the UK.

References

- [1] Jonkman, J., and Martha, D., 2011. "Dynamics of offshore floating wind turbines" analysis of three concepts". *Wind Energy*, **14**, pp. 557–569.
- [2] Bak, C., 2013. "Aerodynamic design of wind turbine rotors". In *Advances in wind turbine blade design and materials*, W. Gentsch and U. Harms, eds., Vol. 47 of *Energy*. Woodhead Publishing, Cambridge, UK, pp. 59–108.
- [3] Sebastian, T., and Lackner, M., 2013. "Characterization of the unsteady aerodynamics of offshore floating wind turbines". *Wind Energy*, **16**(3), pp. 339–352.
- [4] Shem, X., Chen, J., Hu, P., Zhu, X., and Du, X., 2018. "Study of the unsteady aerodynamics of floating wind turbines". *Energy*, **145**, pp. 703–809.
- [5] Wen, B., Dong, X., Tian, X., Peng, Z., Zhang, W., and Wei, K., 2018. "The power performance of an offshore floating wind turbine in platform pitching motion". *Energy*, **154**, pp. 508–521.
- [6] Drofelnik, J., Da Ronch, A., and Campobasso, M., 2018. "Harmonic balance Navier-Stokes aerodynamic analysis of horizontal axis wind turbines in yawed wind". *Wind Energy*, **21**(7), pp. 515–530. DOI: 10.1002/we.2175.
- [7] Bayati, I., Bernini, L., Zanottu, A., Belloli, M., and Zasso, A., 2018. "Experimental investigation of the unsteady aerodynamics of fowt through piv and hot-wire wake measurements". *Journal of Physics: Conference Series*, **1037**.
- [8] Tran, T.-T., and Kim, D.-H., 2015. "The platform pitching motion of floating offshore wind turbine: A preliminary unsteady aerodynamic analysis". *Journal of Wind Engineering and Industrial Aerodynamics*, **142**, pp. 65–81.
- [9] Tran, T.-T., and Kim, D.-H., 2016. "CFD study into the influence of unsteady aerodynamic interference on wind turbine surge motion". *Renewable Energy*, **90**, pp. 204–228.
- [10] Tran, T.-T., and Kim, D.-H., 2016. "Fully coupled aero-hydrodynamic analysis of a semi-submersible fowt using a dynamic fluid body interaction approach". *Renewable Energy*, **92**, pp. 244–261.
- [11] Jonkman, J., and Sprague, M. OpenFAST: An aeroelastic computer-aided engineering tool for horizontal axis wind turbines. <https://nwtc.nrel.gov/OpenFAST>, accessed on 17 March 2020.
- [12] Liu, Y., Xiao, Q., Incecik, A., Peyrard, C., and Wan, D., 2017. "Establishing a fully coupled CFD analysis tool for floating offshore wind turbines". *Renewable Energy*, **112**, pp. 280–301.
- [13] Lienard, C., Boisard, R., and Daudin, C., 2019. Aerodynamic behavior of a floating offshore wind turbine. AIAA paper 2009-269, January. AIAA SciTech Forum, San Diego, California.
- [14] Leble, V., and Barakos, G., 2017. "10-MW Wind Turbine Performance Under Pitching and Yawing Motion". *Journal*

- of Solar Energy Engineering*, **139**, August.
- [15] Campobasso, M., Yan, M., Drofelnik, J., Piskopakis, A., and Caboni, M., 2014. Compressible Reynolds-Averaged Navier-Stokes Analysis of wind Turbine Turbulent Flows Using a Fully Coupled Low-Speed Preconditioned Multigrid Solver. ASME paper GT2014-25562, June.
- [16] Campobasso, M., Sanvito, A., Drofelnik, J., Jackson, A., Zhou, Y., Xiao, Q., and Croce, A., 2018. Compressible Navier-Stokes Analysis of Floating Wind Turbine Rotor Aerodynamics. ASME paper IOWTC2018-1059, November.
- [17] Menter, F., 1994. "Two-equation Turbulence-models for Engineering Applications". *AIAA Journal*, **32**(8), August, pp. 1598–1605.
- [18] Campobasso, M., Piskopakis, A., Drofelnik, J., and Jackson, A., 2013. "Turbulent Navier-Stokes Analysis of an Oscillating Wing in a Power-Extraction Regime Using the Shear Stress Transport Turbulence Model". *Computers and Fluids*, **88**, December, pp. 136–155.
- [19] Campobasso, M., Gigante, F., and Drofelnik, J., 2014. Turbulent Unsteady Flow Analysis of Horizontal Axis Wind Turbine Airfoil Aerodynamics Based on the Harmonic Balance Reynolds-Averaged Navier-Stokes Equations. ASME paper GT2014-25559, June.
- [20] Campobasso, M., Drofelnik, J., and Gigante, F., 2016. "Comparative Assessment of the Harmonic Balance Navier-Stokes Technology for Horizontal and Vertical Axis Wind Turbine Aerodynamics". *Computers and Fluids*, **136**, pp. 345–370.
- [21] Chen, J., Ghosh, A., Sreenivas, K., and Whitfield, D., 1997. Comparison of computations using Navier-Stokes equations in rotating and fixed coordinates for flow through turbomachinery. 35th Aerospace Sciences Meeting and Exhibit, January. Reno, NV, U.S.A.
- [22] Campobasso, M., and Drofelnik, J., 2012. "Compressible Navier-Stokes analysis of an oscillating wing in a power-extraction regime using efficient low-speed preconditioning". *Computers and Fluids*, **67**, August, pp. 26–40.
- [23] Drofelnik, J., and Campobasso, M., 2016. "Comparative Turbulent Three-Dimensional Navier-Stokes Hydrodynamic Analysis and Performance Assessment of Oscillating Wings for Renewable Energy Applications". *International Journal of Marine Energy*, **16**, pp. 100–115.
- [24] Balduzzi, F., Bianchini, A., Gigante, F., Ferrara, G., Campobasso, M., and Ferrari, L., 2015. Parametric and Comparative Assessment of Navier-Stokes CFD Technologies for Darrieus Wind Turbines Performance Analysis. ASME paper GT2015-42663, June.
- [25] Balduzzi, F., Drofelnik, J., Bianchini, A., Ferrara, G., Ferrari, L., and Campobasso, M., 2017. "Darrieus wind turbine blade unsteady aerodynamics: a three-dimensional Navier-Stokes CFD assessment". *Energy*, **128**, pp. 550–563.
- [26] Balduzzi, F., Marten, D., Bianchini, A., Drofelnik, J., Ferrari, L., Campobasso, M., Pechlivanoglou, G., Nayari, C., Ferrara, G., and Paschereit, C., 2018. "Three-Dimensional Aerodynamic Analysis of a Darrieus Wind Turbine Blade Using Computational Fluid Dynamics and Lifting Line Theory". *Journal of Engineering for Gas Turbines and Power*, **140**(2).
- [27] Sanvito, A., Campobasso, M., and Persico, G., 2019. "Assessing the Sensitivity of Stall-Regulated Wind Turbine Power

- to Blade Design Using High-Fidelity CFD”. *Journal of Engineering for Gas Turbines and Power*, **141**(10).
- [28] Campobasso, M., and Baba-Ahmadi, M., 2012. “Analysis of Unsteady Flows Past Horizontal Axis Wind Turbine Airfoils Based on Harmonic Balance Compressible Navier-Stokes Equations with Low-Speed Preconditioning”. *Journal of Turbomachinery*, **134**(6), November.
- [29] Jackson, A., Campobasso, M., and Drofelnik, J., 2018. “Load balance and parallel I/O: Optimising COSA for large simulations”. *Computers and Fluids*, March.
- [30] Le Pape, A., and Lecanu, J., 2004. “3D Navier-Stokes computations of a stall-regulated wind turbine”. *Wind Energy*, **7**, pp. 309–324.
- [31] Turkel, E., 1987. “Preconditioned methods for solving the incompressible and low speed compressible equations”. *Journal of Computational Physics*, **72**, pp. 277–298.
- [32] Weiss, J., and Smith, W., 1995. “Preconditioning applied to variable and constant density flows”. *AIAA Journal*, **33**(11), pp. 2050–2057.
- [33] Campobasso, M., Yan, M., Bonfiglioli, A., Gigante, F., Ferrari, L., Balduzzi, F., and Bianchini, A., 2018. “Low-speed preconditioning for strongly coupled integration of Reynolds-averaged Navier-Stokes equations and two-equation turbulence models”. *Aerospace Science and Technology*, **77**, pp. 286–298.
- [34] Weiss, J., Maruszewski, J., and Smith, W., 1999. “Implicit Solution of Preconditioned Navier-Stokes Equations Using Algebraic Multigrid”. *AIAA Journal*, **37**(1), pp. 29–36.
- [35] Jonkman, J., Butterfield, S., Musial, W., and Scott, G., 2009. Definition of a 5-MW Reference Wind Turbine for Offshore System Development. Tech. Rep. NREL/TP-500-38060, NREL, Golden, CO, USA.
- [36] Campobasso, M., Cavazzini, A., and Minisci, E., 2020. “Rapid Estimate of Wind Turbine Energy Loss due to Blade Leading Edge Delamination Using Artificial Neural Networks”. *Journal of Turbomachinery*, **142**(7), July.
- [37] Castorrini, A., Cappugi, L., Bonfiglioli, A., and Campobasso, M., 2020. Assessing wind turbine energy losses due to blade leading edge erosion cavities with parametric cad and 3d cfd. paper 2020-88. TORQUE Conference, Delft, The Netherlands.
- [38] Chow, R., and van Dam, C., 2012. “Verification of computational simulations of the NREL 5 MW rotor with a focus on inboard flow separation”. *Wind Energy*, **15**, pp. 967–981.
- [39] Nejad, A., Bachynski, E., and Moan, T., 2019. “Effect of Axial Acceleration on Drivetrain Responses in a Spar-Type Floating Wind Turbine”. *Journal of Offshore Mechanics and Arctic Engineering*, **141**(3), June.
- [40] Ortolani, A., Persico, G., Drofelnik, J., Jackson, A., and Campobasso, M., 2020. Cross-comparative analysis of loads and power of pitching floating offshore wind turbine rotors using frequency-domain Navier-Stokes CFD and blade element momentum theory. paper 2020-89. TORQUE Conference, Delft, The Netherlands.
- [41] Glauert, H., 1928. “The effect of compressibility on the lift of an aerofoil”. *Proceedings of the Royal Society A: Mathematical, Physical and Engineering Sciences*, **118**, March, pp. 113–119.
- [42] Cavazzini, A., Campobasso, M., Marconcini, M., Pacciani, R., and Arnone, A., 2019. “Harmonic balance Navier-Stokes analysis of tidal stream turbine wave loads”. In *Recent Advances in CFD for Wind and Tidal Offshore Turbines*,

E. Ferrer and A. Montlaur, eds., Springer Tracts in Mechanical Engineering. Springer International Publishing. ISBN 978-3-030-11887-7.